Inorganic Chemistry

Article

pubs.acs.org/IC

Tuning the Functionality of a Carbon Nanofiber–Pt–RuO_2 System from Charge Storage to Electrocatalysis

Beena K. Balan and Sreekumar Kurungot*

Physical and Materials Chemistry Division, National Chemical Laboratory, Pune 411 008, India

Supporting Information

ABSTRACT: Chemical-functionalization-induced switching in the property of a hybrid system composed of a hollow carbon nanofiber (CNF) and Pt and RuO_2 nanoparticles from charge storage to electrocatalysis is presented. The results of this study show how important it is to have a clear understanding of the nature of surface functionalities in the processes involving dispersion of more than one component on various substrates including carbon nanomorphologies. When pristine CNF is used to decorate Pt and RuO_2 nanoparticles, random dispersion occurs on the CNF surface (C-PtRuO_2). This results in mainly phase-separated nanoparticles rich in RuO_2 characteristics. In contrast to this, upon moving from the pristine CNF to those activated by a simple H_2O_2 treatment to create oxygen-containing surface functional groups, a material rich in Pt features on the surface is obtained (F-PtRuO_2). This is achieved because of the preferential adsorption of RuO_2 by the functionalized surface of CNF. A better affinity of the oxygen-containing functional groups on CNF toward RuO_2 mobilizes relatively faster adsorption of this moiety, leading to a well-controlled segregation of Pt nanoparticles toward the surface. Further reorganization of Pt nanoparticles leads to the formation of a Pt nanosheet structure on the surface. The electrochemical properties of these materials are initially evaluated using cyclic voltammetric analysis. The cyclic voltammetric results indicate that C-PtRuO_2 shows a charge storage property, a typical characteristic of hydrous RuO_2, whereas F-PtRuO_2 shows an oxygen reduction property, which is the characteristic feature of Pt. This clear switch in the behavior from charge storage to electrocatalysis is further confirmed by galvanostatic charge–discharge and rotating-disk-electrode studies.

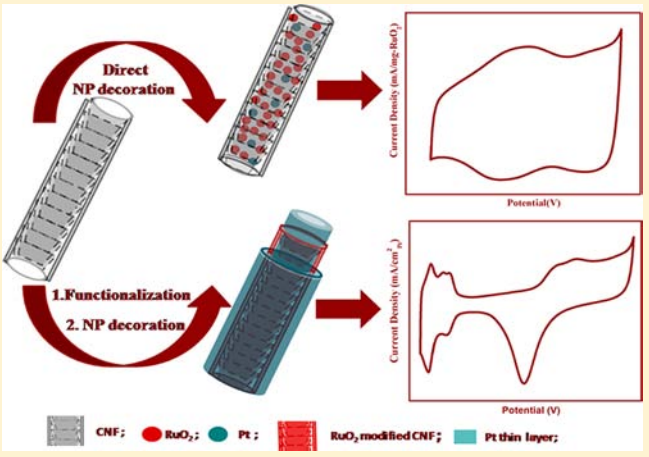

INTRODUCTION

Imparting surface-sensitive functions in high-aspect-ratio one-dimensional carbon nanostructures like nanotubes and nanofibers is a demanding challenge considering their myriad applications in a variety of fields ranging from nanoelectronics to biomedical devices.[1−3] The urge for such modifications originates from their inherent limitations like poor processability, reactivity, and solubility.[4,5] In a broad way, the approaches commonly adopted to put up such improvements can be classified into two: endohedral or functionalization from the inside and exohedral or functionalization from the outside.[6,7] Even though, from a basic chemistry point of view, functionalization is a simple means of recuperating the physicochemical properties of carbon nanotubes (CNTs) or carbon nanofibers (CNFs), the probable utility of functionalization commences from the simple unroping of the nanotube bundles to the highly specific grafting of single-stranded DNA for the selective and sensitive recognition of cDNA.[8,9]

Nanostructured materials, in general, have great advantages over their bulk counterparts. Single-phased nanomaterials, however, may not be able to fulfill all of the requirements. Assembling several functional nanomaterials into a single material is a logical way to surpass the above limitations because the collective interaction between the constituents results in novel and unique properties.[10,11] However, the success of such a hybrid design, in fact, depends on the selection of the proper individual components and the choice of suitable methods to assemble the nanocomponents into the desired nanostructures.

In view of the growing importance of designing nanostructured hybrid materials, herein we report the simple covalent functionalization as an efficient strategy to fine-tune the properties of a hybrid system composed of Pt, RuO_2, and a hollow CNF from charge storage to electrocatalysis. Initially, a modified polyol process by adjustment of the wettability and surface tension of the solvent medium by using an ethylene glycol–water solution containing Pt^{4+} and Ru^{3+} ions was adopted for metal decoration on CNF.[12] Because of the peculiar morphological features and the active terminal graphene edges in the inner cavity of CNF, the nanoparticles are selectively dispersed in the inner cavity when CNF is used.

Received: May 31, 2012
Published: September 4, 2012

dx.doi.org/10.1021/ic301147s | Inorg. Chem. 2012, 51, 9766–9774

However, in a second case, CNF is first functionalized (FCNF) to create oxygen-containing functional groups along the inner and outer surfaces of CNF. This results in dispersion of the nanoparticles on both surfaces of FCNF. Along with this, significant differences in the dispersion characteristics are also observed. Because the Ru ion has a higher affinity for oxygen than the Pt ion, preferential adsorption of the Ru ion on FCNF through the oxygen-containing functional group occurs.[13] The Pt ions remaining in the solution will be adsorbed by filling the vacant spaces either on FCNF or directly over the adsorbed Ru ions in the case of the fully filled state. In a recent report, we demonstrated that, at a Pt:Ru atomic composition of 1:5, Ru formed a complete layer in the inner cavity as well as on the outer walls. In the present study, we used the Pt:Ru atomic composition of 1:5 for ensuring complete exposure of Pt to the surface.[14] These adsorbed ions, during reduction, form a thin layer of Pt selectively exposed to the surface of FCNF with a RuO_2 layer in between. Thus, with the same composition of Pt and RuO_2, two distinctly different distribution characteristics could be realized: when pristine CNFs are used to assemble the nanoparticles, mainly monometallic, phase-separated nanoparticles rich in RuO_2 characteristics are obtained, whereas FCNF leads to a material rich in Pt features. This architectural tuning is a result of the controlled and predictable assembly of ions based on the preferential adsorption of one metal ion over the other due to the presence of oxygen-containing functional groups. The electrochemical analysis of these samples using cyclic voltammetry, galvanostatic charge−discharge, and rotating-disk-electrode studies shows a switch in the property from charge storage to electrocatalysis for the same composition while moving from pristine CNF to FCNF. Moreover, although hydrous RuO_2 has been reported for its enhanced charge storage capabilities and Pt for its magnificent electrocatalytic properties, while considering them matriculately separate, we also demonstrate that the individual characteristics of both systems mutually benefit by the second counterpart. The different steps involved in the synthesis of both materials are systematically represented in Scheme 1.

EXPERIMENTAL SECTION

Materials. Hydrogen hexachloroplatinate hexahydrate ($H_2PtCl_6{\cdot}6H_2O$) and ruthenium chloride ($RuCl_3$) were purchased from Aldrich Chemicals. Ethylene glycol (EG) and sulfuric acid (H_2SO_4) were procured from Rankem Chemicals. All of the chemicals were used as received without any further purification. Poly(tetrafluoroethylene) filter paper (pore size, 0.45 μm; Rankem) was used for filtration. A 200 mesh carbon-coated copper grid (Ted Pella, Inc.) was used for the high-resolution transmission electron microscopy (HRTEM) observations.

Scheme 1. Formation Mechanism of Pt-RuO_2 Bimetallic Nanoparticles on Pristine and Functionalized CNF

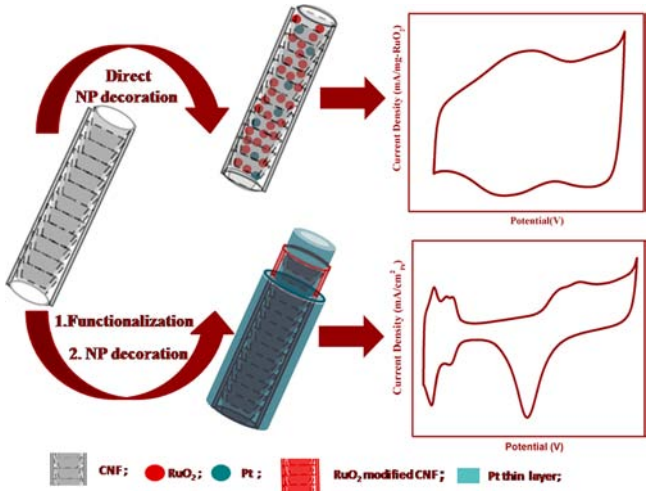

Functionalization of Carbon Supports. To prepare FCNF by functionalization of the substrate, 1 g of pristine CNF was well dispersed in 200 mL of 30% H_2O_2. This was then refluxed at a temperature of 60 °C for 5 h. Subsequently, the mixture was filtered, washed with deionized water, and dried.

Preparation of CNF-Supported Catalysts. Both catalysts (i.e., by using CNF and FCNF respectively as the substrates) with 20 wt % loading (15 wt % RuO_2 and 5 wt % Pt) were prepared using the coreduction of $H_2PtCl_6{\cdot}6H_2O$ and $RuCl_3$ in the polyol−water mixture. The modification of the polyol process by using a proper composition of polyol and water was a critical step to achieve the nanoparticle decoration in the inner cavity as well. This is attained by tuning the surface tension and polarity characteristics of the solvent medium to facilitate the reactant entry into the tubular region and homogeneous wetting of the inner wall surface by the solvents.

In a typical synthesis, the required amount of CNF was added to an aqueous EG solution corresponding to an EG−H_2O volume ratio of 3:2 and the content was well dispersed by sonication. In the next step, a similar aqueous EG solution of the Pt and Ru precursors was added drop by drop with stirring. Subsequently, the mixture was kept under stirring for 5 h at ambient temperature to achieve well dispersion of the components in the mixture. After this aging process, the mixture was refluxed at 140 °C for 5 h. The solid material was then collected by filtration, washed with water, and dried under vacuum to obtain the samples C-PtRuO_2. The same procedure was adopted for the synthesis of F-PtRuO_2 also, where FCNF was used instead of CNF. This aging time in the synthesis procedure is a key parameter because the precursor solution has to be reached inside the tubes of the support material, which has straw-type morphology. Hence, both C-PtRuO_2 and F-PtRuO_2 were allowed to age for 5 h. This is also important for allowing reorganization of the Pt and Ru ions to achieve preferential adsorption of the Ru ions in the case of FCNF as the substrate. For comparison, pure Pt and pure RuO_2 catalysts supported on FCNF and RuO_2 supported on CNF were also prepared using the corresponding Pt and Ru precursors, respectively, denoted as F-Pt, F-RuO_2, and C-RuO_2.

Characterization. HRTEM coupled with energy-dispersive X-ray (EDX) analysis was performed on a TECNAI-T 30 model instrument equipped with an EDX attachment operated at an accelerating voltage of 300 kV. Samples for HRTEM imaging were prepared by placing a drop of the catalyst sample in isopropyl alcohol onto a carbon-coated copper grid (3 nm thickness, deposited on a commercial copper grid for electron microscopy). This is then dried in air and loaded into the electron microscopic chamber. X-ray diffraction (XRD) was conducted using a Philips X'pert pro powder X-ray diffractometer operating with Cu Kα radiation (λ = 0.15406 nm, Ni filter) generated at 40 kV and 30 mA. Thermogravimetric analysis (TGA) was performed on a SDT Q600 TG-DTA analyzer. X-ray photoelectron spectroscopy (XPS) measurements were carried out on a VG MicroTech ESCA 3000 instrument at a pressure of >1 × 10^{-9} Torr (pass energy of 50 eV; electron takeoff angle 60°) using monochromatic Mg Kα (source, $h\nu$ = 1253.6 eV). The overall resolution of the instrument was ~1 eV. Alignment of the binding energy (BE) was carried out using an Au 4f BE of 84 eV as the reference. The BE of the C 1s peak was fixed to 284.5 eV, and all peaks were calibrated with reference to this graphitic C 1s peak. The background was subtracted by the Shirley method. The spectra were fitted using a combined polynomial and Shirley-type background function.

Electrochemical Studies. All of the electrochemical analyses were performed on an Autolab PGSTAT30 (Eco Chemie) instrument. A conventional three-electrode test cell was used for the cyclic voltammetric (CV) and rotating-disk-electrode (RDE) studies. A glassy carbon (GC) electrode with a geometric area of 0.196 cm^2 (Pine

dx.doi.org/10.1021/ic301147s | Inorg. Chem. 2012, 51, 9766−9774

Instruments) coated with the sample was used as the working electrode (WE). $Hg/HgSO_4$ and Pt foil were used as the reference and counter electrodes, respectively. The WE for the CV and RDE studies was prepared as follows. A total of 5 mg of the catalyst was well dispersed in 1 mL of isopropyl alcohol. Then 10 μL of the above slurry was drop-coated on the GC electrode using a micropipet. A total of 2 μL of a 0.01 wt % Nafion solution in ethanol was used as the binder. This electrode was then dried in air. An aqueous solution of 0.5 M H_2SO_4 was used as the electrolyte for normal CV and RDE studies. For methanol oxidation, a mixture of 1 M CH_3OH and 0.5 M H_2SO_4 was used. The CV measurement was taken at a scan rate of 50 mV/s. RDE studies were conducted at various rotating speeds, i.e., 400, 900, 1200, 1600, and 2500 rpm, with a constant scan rate of 5 mV/s. The galvanostatic charge−discharge measurements were done using a Solatron SI1287 electrochemical interface with Carware software at different current densities in a two-electrode configuration. The electrodes for the capacitance measurements were prepared by coating the respective materials on a carbon paper having an electrode area of 1 × 1 cm^2 followed by drying at 120 °C in a vacuum oven. For the preparation of the slurry, 90% of the active material and 10% of the Nafion binder were used. The material loading on the electrode was kept as 2 mg/cm^2.

RESULTS AND DISCUSSION

Structural and Morphological Characterization. HRTEM analysis is used for the morphological characterization of the CNF support as well as the CNF/FCNF-Pt-RuO_2 hybrid materials. From the HRTEM images of the CNF support given in Figure 1, it is clear that CNF has a large central hollow core and open tips. The open tips are circled in Figure 1a. Figure 1b, which is an enlarged view of a single CNF, clearly depicts that unlike CNTs, which are made by the simple rolling of graphene sheets, this material is made up of truncated conical graphene layers. Because of this peculiar rolling of graphene sheets, CNF exhibits a large central hollow core, which, in turn, imposes a significant portion of exposed and reactive edges in the inner channel created within the CNF, as highlighted in the blue box. However, the edge sites on the outer surface of CNF are clearly covered by deposition of a pyrolitic carbon layer induced by the high reaction temperature used for the synthesis of this material (marked in the red box). This peculiar morphology of the material leaves its inner wall inherently active and outer wall inert.[15−17] However, many researchers have reported that this inactive outer wall can be activated by suitable chemical pretreatments. Hence, the relatively large inner-diameter, open tips, active inner wall and the possibility of activating the inert outer wall by chemical treatments make this a potential support material for effectively dispersing various nanoparticles both on the outer walls and in the inner cavity.

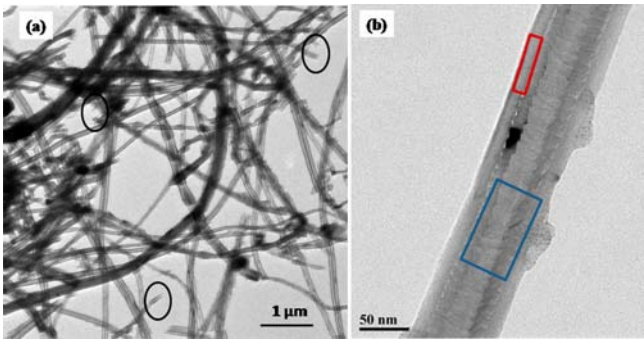

Figure 1. HRTEM images of (a) the CNF support with circled regions representing the open tips of the CNF support and (b) a single CNF clearly depicting the active terminal graphene edges and the deactivated outer wall due to the deposition of a pyrolitic carbon layer.

HRTEM analysis is further used to confirm the nanoparticle decoration on CNF and FCNF, and the images shown in Figure 2 provide direct evidence to the proposed mechanism of the formation of the hybrid structures, as shown in Scheme 1. Figure 2a, which corresponds to the low-magnification HRTEM image of F-$PtRuO_2$, clearly indicates the uniform and excellent distribution of nanoparticles on the outer wall as well as in the inner cavity of FCNF. Interestingly, the low-magnification image of C-$PtRuO_2$ given in Figure 2d confirms that the nanoparticles are exclusively present in the inner cavity only and the outer wall is completely free. The average particle size and distribution were also determined from the HRTEM images assuming a spherical shape for the particles. At least 250 particles were selected randomly from different micrographs for each sample. The corresponding particle-size distribution histogram obtained for F-$PtRuO_2$ and C-$PtRuO_2$ is given in parts c and f of Figure 2, respectively. It is found that the average particle size of the nanoparticles in F-$PtRuO_2$ is 2.6 ± 0.9 nm, whereas this is almost doubled in the case of C-$PtRuO_2$, which is 5.5 ± 0.9 nm. This observed reduction in the size of the nanoparticles while moving from pristine to pretreated CNF can be attributed to almost double the surface area (both the inner cavity and outer walls) made available in FCNF as a result of functionalization.

Although the low-magnification image displayed almost similar features in terms of dispersion, upon moving to higher magnification, some differences were observed in the assembly of the nanoparticles. F-$PtRuO_2$ displayed a continuous layer formed by the assembly of a large number of fine nanoparticles (Figure 2b). This assembly formation was further confirmed from the highly oriented grains compared to the misoriented grains in C-$PtRuO_2$ (Figure 2e). Apart from this, the average *d* spacing measured in the case of F-$PtRuO_2$ was 2.2 Å, which corresponded to the (111) plane of face-centered-cubic (fcc) Pt. In addition to the *d* spacing, the angle between the observed planes was also measured, which was ca.127.8°. This value was in close agreement with that reported for the angle between the Pt(111) and Pt(100) planes.[18] The absence of the lattice fringes corresponding to RuO_2 supplemented by the measured angle between the observed planes indicated that Pt was selectively exposed to the surface in F-$PtRuO_2$. In contrast to this, C-$PtRuO_2$, as already discussed, displayed separate nanoparticles with a distinct boundary (Figure 2e). The lattice spacings of more than 100 nanoparticles were measured to ensure statistically significant representation, and this gave a *d* value of 2.2 Å corresponding to the (111) plane of fcc Pt, as highlighted by the red circles in Figure 2e. The lattice spacing corresponding to RuO_2 cannot be measured because of its amorphous nature and the vague contrast (highlighted by blue circles in Figure 2e). A similar narrow contrast was observed in the HRTEM image of pure RuO_2 nanoparticles supported on FCNF (F-RuO_2) also (Figure 2g,h). The particle-size distribution obtained for F-RuO_2 is presented in Figure 2i. These features clearly indicate the formation of phase-separated monometallic nanoparticles. Apart from this, the extent of atomic level resolution observed in F-$PtRuO_2$ was extraordinarily high compared to that in C-$PtRuO_2$. This was evidenced by the coexistence of two lattice planes, i.e., (111) and (100), in F-$PtRuO_2$, while in C-$PtRuO_2$, only the fringes corresponding to the (111) plane were observed. This observation also validated the fact that a thin layer was formed in the case of F-

dx.doi.org/10.1021/ic301147s | Inorg. Chem. 2012, 51, 9766−9774

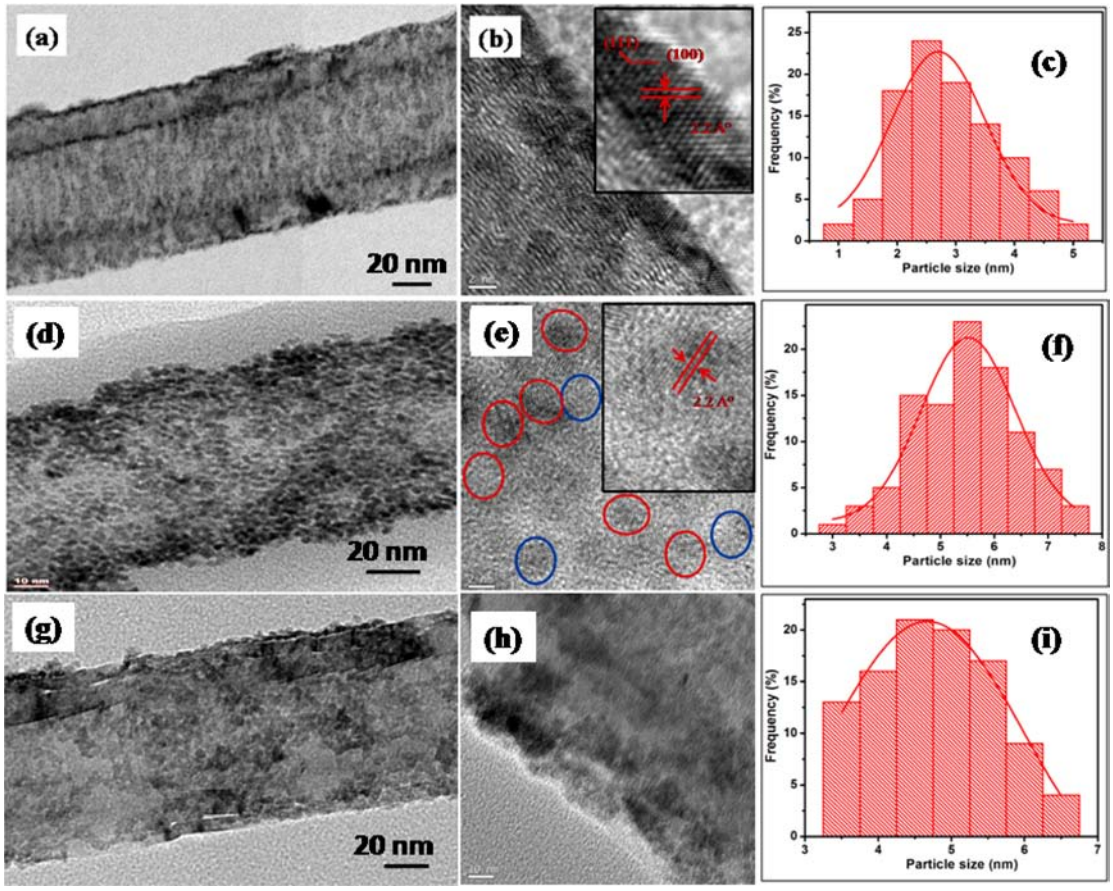

Figure 2. (a) HRTEM image of F-$PtRuO_2$ showing the presence of nanoparticles in the inner cavity and outer wall of FCNF, (b) image clearly indicating the formation of a thin layer of Pt with highly oriented grains, (d) image of CNF decorated with nanoparticles only in the inner cavity (C-$PtRuO_2$), (e) image showing the fine distribution of phase-separated monometallic nanoparticles, with the inset of b and e showing the *d* spacing and angle between the planes, (g) image of F-RuO_2 depicting the nanoparticle decoration on both walls of FCNF, and (h) high-magnification image of F-RuO_2 clearly indicating its amorphous character. (c, f, and i) Histograms of the particle size for F-$PtRuO_2$, C-$PtRuO_2$, and F-RuO_2, respectively.

$PtRuO_2$. EDX analysis of F-$PtRuO_2$ and C-$PtRuO_2$ was also conducted, and the results are presented in the Supporting Information, parts a and b of Figure S1, respectively. The EDX analysis results indicated the presence of Pt and Ru in both samples. The Pt:Ru atomic percentage obtained for F-$PtRuO_2$ and C-$PtRuO_2$ from EDX analysis was 1:3.91 and 1:4.84, respectively, which were close to the initial precursor percentage of 1:5. However, the total loading of Pt and Ru calculated from EDX analysis was less than the actual metal loading. This could be due to the carbon and copper contribution from the TEM grid used for analysis.

XRD was used to characterize the crystal structure of the materials, and accordingly Figure 3a shows a comparison of the XRD patterns of CNF, C-$PtRuO_2$, and F-$PtRuO_2$. As shown in Figure 3a, the pristine CNF has two diffraction peaks: a high intense (002) peak at $2\theta = 26.4°$ and a low intense (100) peak at $2\theta = 43°$. Of interest, two broad peaks characteristic of amorphous RuO_2 appeared between $2\theta = 30$ and 40° and 50 and 65° in both C-$PtRuO_2$ and F-$PtRuO_2$ apart from the peaks corresponding to the CNF support. However, the peaks corresponding to Pt cannot be detected in both samples, which can be attributed to the lack of sufficient scattering matter (Pt) in the material.[19]

The surface chemical composition of these materials was evaluated by XPS analysis. Accordingly, Figure 3b shows a comparison of the full survey XP spectra obtained for C-$PtRuO_2$ and F-$PtRuO_2$ before deconvolution. A sharp peak observed at a BE of 284.6 eV in both C-$PtRuO_2$ and F-$PtRuO_2$ is attributed to the C 1s peak of the CNF. The peak at the BE of 531.4 eV indicates the presence of oxygen, and more fascinatingly, the intensity of this peak is significantly high in F-$PtRuO_2$ compared to that in C-$PtRuO_2$. This gives lucid evidence for the extent of functionalization effected in the CNFs as a result of H_2O_2 treatment.[20] Because the most intense 3d levels of Ru merge with the intense C 1s peak in the spectrum, it is very difficult to perceive its presence before deconvolution. Apart from all of these observations, a remarkable discrepancy was observed in the Pt 4f region. In F-$PtRuO_2$, a clear doublet corresponding to Pt was observed at a BE of 73.4 eV.[21] In sharp contrast to this, no signatures for Pt was observed in the XP spectra of C-$PtRuO_2$. However, in the TGA results obtained in air from room temperature to 1000 °C, presented in Figure 3c, all of the materials displayed almost similar TGA profiles, i.e., an initial small weight loss followed by a continuous decay. From the residue content, it was concluded that the metal content present in the CNF was close to zero and the material loadings in C-$PtRuO_2$ and F-$PtRuO_2$ were ca. 17.5 and 17 wt %, respectively. Hence, from a combination of the XPS and TGA results, it was inferred that, in both materials, Pt and RuO_2 were present and were close to the estimated amounts from the initial precursor amount taken, and the incongruity observed in the Pt region gives unambiguous

dx.doi.org/10.1021/ic301147s | *Inorg. Chem.* 2012, 51, 9766−9774

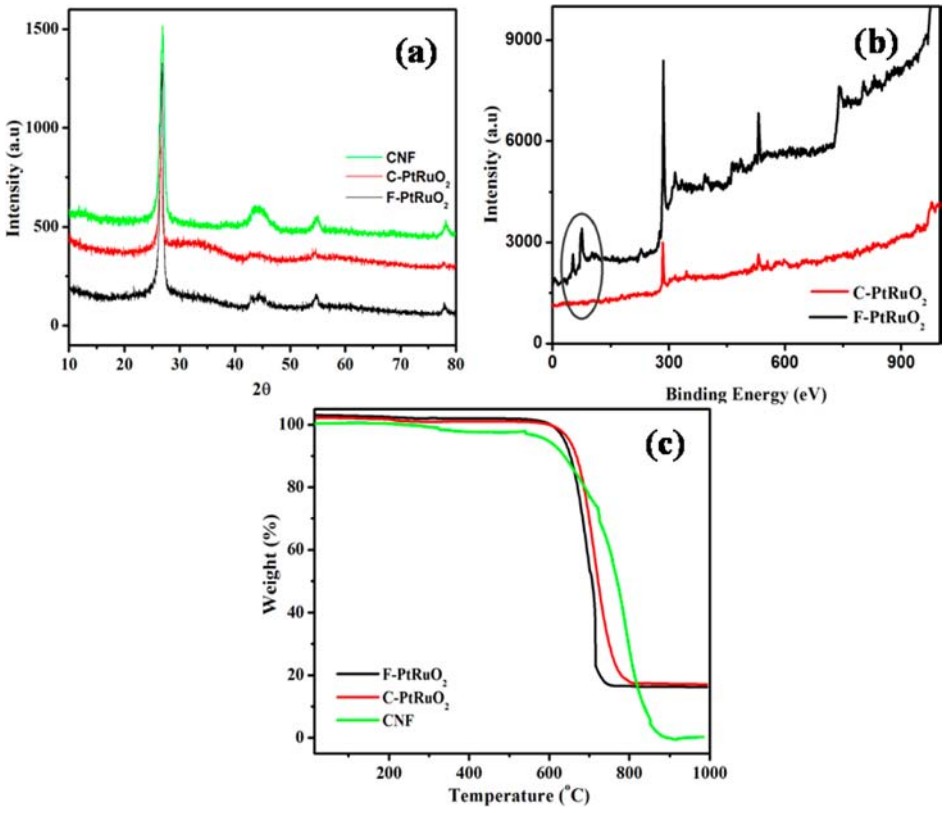

Figure 3. (a) XRD patterns obtained for C-$PtRuO_2$, F-$PtRuO_2$, and CNF. (b) Comparison of the full survey XP spectra of C-$PtRuO_2$ and F-$PtRuO_2$ before deconvolution. (c) TGA profile obtained for C-$PtRuO_2$, F-$PtRuO_2$, and CNF in air from room temperature to 1000 °C.

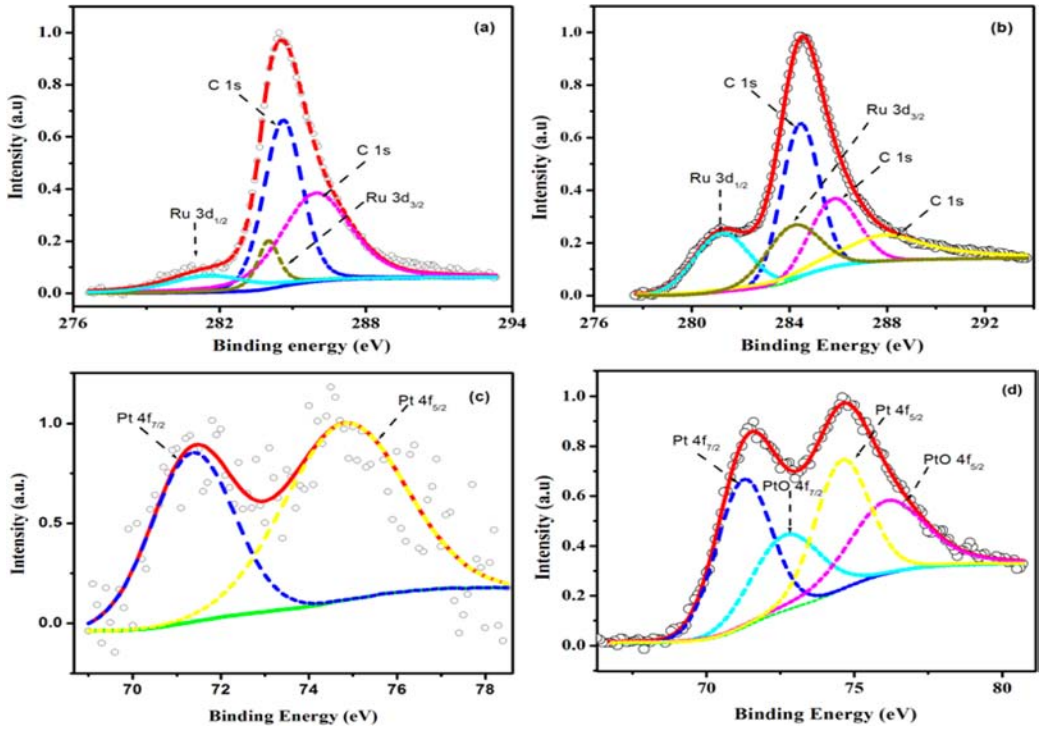

Figure 4. XPS spectra of C 1s and Ru 3d core levels of (a) C-$PtRuO_2$ and (b) F-$PtRuO_2$. (c and d) Respectively the Pt 4f levels in C-$PtRuO_2$ and F-$PtRuO_2$ after deconvolution. The circles represent the experimental data, the red line represents the fitting data for the overall signal, and the dotted lines are the deconvoluted individual peaks for different species present in the sample.

evidence for the selective exposure of Pt to the surface in F-$PtRuO_2$.

To gain more insights into the surface structures and the mode of interaction between the individual components, various parts of the XP spectra of both samples were

dx.doi.org/10.1021/ic301147s | Inorg. Chem. 2012, 51, 9766−9774

deconvoluted. A comparison of the deconvoluted C 1s part given in Figure 4 reveals the following features. In C-PtRuO$_2$, the carbon region shows four peaks at 284.6, 285.9, 281.6, and 284 eV (Figure 4a), which can be assigned to the graphitic carbon, carbon bonded to −OH groups, and $3d_{1/2}$ and $3d_{3/2}$ levels of Ru, respectively. In F-PtRuO$_2$, the respective peaks are observed at 284.5, 285.9, 281.3, and 283.9 eV, with one additional peak at 287.8 eV (Figure 4b) corresponding to the carbon bonded to −COOH groups. From the observed peak positions, it is evident that Ru is present in the form of RuO$_2$ in both hybrids and no pure metallic Ru is detected.[22] The intensity of the peak corresponding to C−OH is also enhanced to a noticeable extent in F-PtRuO$_2$ compared to that in C-PtRuO$_2$. The occurrence of the additional peak with respect to −COOH groups and the enhancement in the intensity of the peak corresponding to C−OH groups corroborate the extent of functionalization effected in CNFs as a result of H_2O_2 treatment. This is further confirmed from the IR spectroscopy results presented in Figure S2, Supporting Information.

The Pt 4f levels in C-PtRuO$_2$, after deconvolution, give one doublet at BEs of 71.3 and 74.8 eV, which correspond to the Pt $4f_{7/2}$ and $4f_{5/2}$ levels, respectively, as shown in Figure 4c. From the peak position and the peak-to-peak separation, it can be concluded that Pt is present in the zero oxidation state in C-PtRuO$_2$. Interestingly, from Figure 4d, it can be clearly manifested that deconvolution of the Pt 4f levels of F-PtRuO$_2$ results in two doublets. The doublet at 71.2 and 74.5 eV corresponds to the regular peaks with respect to Pt in the zero oxidation state. The additional doublet observed at 72.6 and 76.2 eV corresponds to Pt in the higher oxidation states. However, it is interesting to note that this high-BE doublet matches neither with the Pt in the zero oxidation state nor with the pure platinum oxide and falls somewhere between these two. This observed intermediate value of the BE indicates that the doublet is a result of the slight oxidic character imparted to the Pt. Consequently, the peaks corresponding to the Pt in the zero as well as in the higher oxidation states and the perceived shift in its peak position compared to the reported values lean toward the possible interaction between Pt and RuO$_2$ in F-PtRuO$_2$.[23,24] In contrast to this, the peaks corresponding to Pt in the higher oxidation state are absent in C-PtRuO$_2$, and this excludes any strong interaction between Pt and RuO$_2$. This observation is in excellent agreement with the HRTEM results, where well-separated, monometallic Pt and RuO$_2$ nanoparticles are observed in C-PtRuO$_2$, whereas a highly oriented, thin layer of Pt is detected in F-PtRuO$_2$. Moreover, from the signal-to-noise ratio of the Pt spectra, it is evident that the Pt peaks are attenuated from the higher RuO$_2$ content in C-PtRuO$_2$, while intense Pt peaks are observed for F-PtRuO$_2$. Further, the surface atomic composition of C-PtRuO$_2$ and F-PtRuO$_2$ is also calculated from the XPS results and is given in Table 1. It is evident from Table 1 that the Pt:Ru atomic percentages obtained for C-PtRuO$_2$ and F-PtRuO$_2$ are respectively 1:4.7 and 1:4.0, resulting in a surface composition of 26.6% Pt and 73.4% Ru in C-PtRuO$_2$ and 30.5% Pt and 69.5% Ru in F-PtRuO$_2$. The surface composition calculated from the XPS data for C-PtRuO$_2$ is close to the initial composition of 25% Pt and 75% Ru calculated from the precursor amounts. However, it is important to note that the surface composition obtained for F-PtRuO$_2$ from the XPS quantification shows a slight increase in the % Pt compared to the initial composition. This could be due to the selective exposure of Pt to the surface in F-PtRuO$_2$. Accordingly, on the basis of a combination of the results from HRTEM, XRD, XPS, and TGA, it can be concluded that Pt is selectively exposed to the surface in F-PtRuO$_2$, while well-separated monometallic nanoparticles are present in C-PtRuO$_2$ and such a desirable nanoscale architectural tuning is a result of the preferential adsorption of one metal ion over the other.

Table 1. Surface Composition Quantification from XPS

	peak position (eV)			relative weight percentage (wt %)		
sample	C	Ru	Pt	Ru	Pt	Pt:Ru atomic ratio
F-PtRuO$_2$	284.5	281.3	71.2	69.5	30.5	1:4
	285.9		74.5			
	287.8	283.9	72.6			
			76.2			
C-PtRuO$_2$	284.6	281.6	71.3	73.4	26.6	1:4.7
	285.9	284	74.8			

Electrochemical Characterization. To investigate the influence of such architectural tuning on the property modulation, electrochemical responses of these materials were initially evaluated using CV analysis. For the electrochemical experiments, 10 μg of the material was loaded onto a GC electrode. A comparison of the cyclic voltamograms obtained for C-PtRuO$_2$ and F-PtRuO$_2$ in 0.5 M H_2SO_4 at a scan rate of 50 mV/s is given in parts a and b of Figure 5, respectively. The CV response of C-PtRuO$_2$ in Figure 5a exhibits almost a rectangular shape, which is a typical characteristic of a capacitor-like material. The presence of RuO$_2$ in the material is supposed to contribute pseudocapacitance and, as expected, wide redox peaks, which are the distinctiveness of the hydrous ruthenium oxide, are observed in the cyclic voltamogram.[25] Of interest, no specific features with respect to Pt were observed in the CV loop. The rectangular shape of the CV loop of the material indicates low contact resistance in the system.[26] It is interesting further that the rectangular shape of the cyclic voltamogram was maintained even at various scan rates. Apart from this, the capacitance current of the electrode increased with increasing scan rate (Figure S3, Supporting Information), which indicates excellent capacitance behavior and low contact resistance in the material. The specific capacitance of this material was calculated at a scan rate of 50 mV/s, and the capacitance obtained with respect to the RuO$_2$ loading was 1100 F/g. Considering the fact that the specific capacitance obtained for FCNF at the same loading was 15 F/g only (Figure S4, Supporting Information), almost the entire capacitance obtained can be ascribed to the RuO$_2$ moiety itself. Galvanostatic charge−discharge studies were also conducted in 0.5 M H_2SO_4 in the potential window of 0−1 V to confirm the capacitive behavior of C-PtRuO$_2$. Accordingly, the charge−discharge profile obtained at different charging currents, i.e., 1, 2, 3, and 5 A/g, is shown in Figure 5c. The charge−discharge profile is linear and symmetric in the entire range of potential, indicating its excellent capacitive behavior. The specific capacitance of C-PtRuO$_2$ calculated with respect to the RuO$_2$ loading from the charge−discharge data at the current density of 1 A/g was 1020 F/g, which is in excellent agreement with the capacitance value obtained from the CV results.

On the other hand, the CV response of F-PtRuO$_2$ presented in Figure 5b shows distinctly different features. The cyclic voltammogram obtained is similar to that of a polycrystalline Pt electrode with characteristic current peaks that can be ascribed

dx.doi.org/10.1021/ic301147s | Inorg. Chem. 2012, 51, 9766−9774

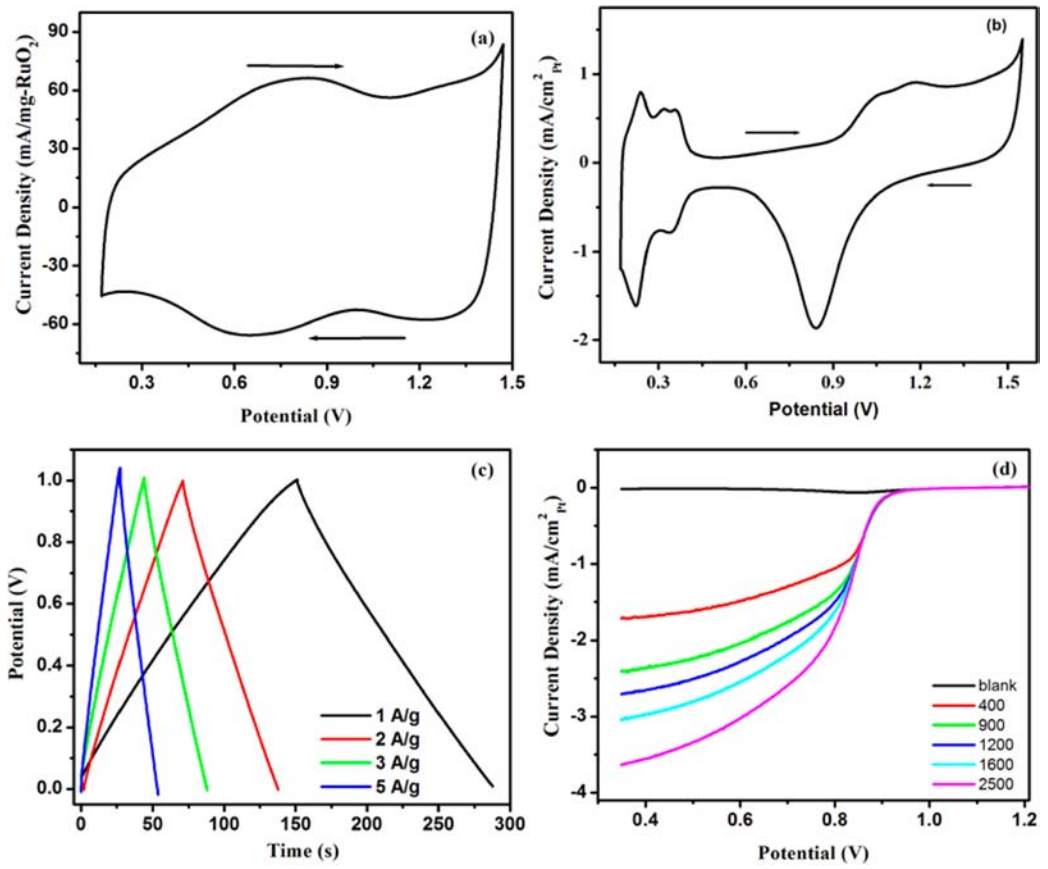

Figure 5. Comparison of cyclic voltammograms of (a) C-$PtRuO_2$ and (b) F-$PtRuO_2$ at a scan rate of 50 mV/s. (c) Galvanostatic charge−discharge curves of the C-$PtRuO_2$ electrode at different charging currents from 1 to 5 A/g. (d) ORR polarization curves for F-$PtRuO_2$ at a sweep rate of 5 mV/s at various rotation rates. The electrolyte 0.5 M H_2SO_4 solution and all of the potentials are quoted vs NHE.

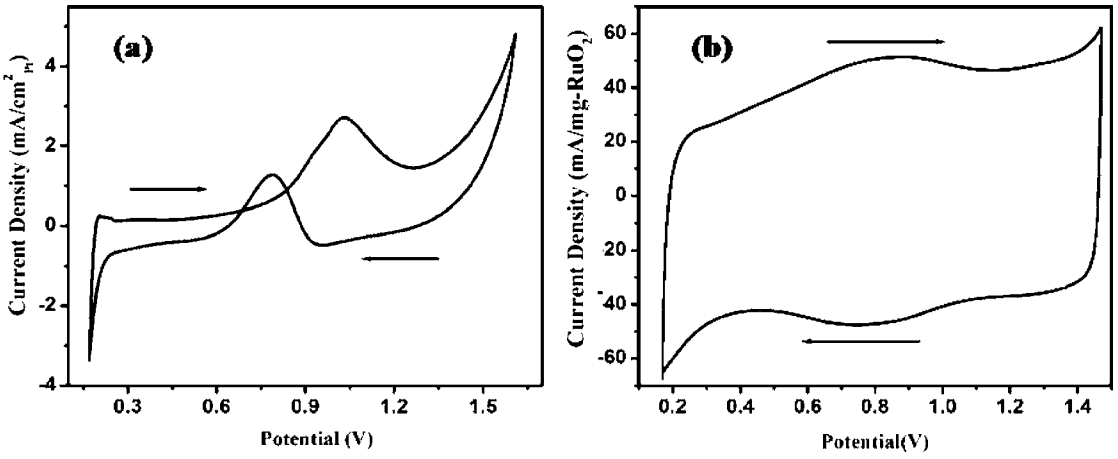

Figure 6. Cyclic voltammograms for the methanol oxidation reaction of (a) F-$PtRuO_2$ and (b) C-$PtRuO_2$. Electrolyte 0.5 M H_2SO_4 + 1 M CH_3OH, scan rate 50 mV/s; all of the potentials are quoted vs NHE.

to the hydrogen adsorption−desorption and peaks corresponding to surface oxide formation and reduction.[27] The electrochemically active area (ECSA), which decides the actual catalytic activity of a material, was calculated by measuring the Coulombic charge for desorption of the monolayer of hydrogen, and the ECSA obtained for F-$PtRuO_2$ was 384 cm^2/mg of Pt. Linear sweep voltammetric analysis of F-$PtRuO_2$ in an oxygen-saturated aqueous 0.5 M H_2SO_4 solution with various rotating rates at a 5 mV/s scan rate was also performed. The results presented in Figure 5d indicate that the limiting current densities of the oxygen reduction reaction (ORR) were progressively increased with the rotating rate. It can be ascribed to the increase in the mass-transfer rate of the dissolved oxygen from the bulk solution to the electrode surface. Apart from this, the onset potential for ORR obtained for F-$PtRuO_2$ was 0.84 V vs NHE. This value is also comparable with other Pt-based catalysts reported in the literature.[28] All of these features indicate the oxygen reduction activity of F-$PtRuO_2$ material. Hence, the above observations manifest the clear transition from the typical capacitance characteristic of RuO_2 to the

dx.doi.org/10.1021/ic301147s | Inorg. Chem. 2012, 51, 9766−9774

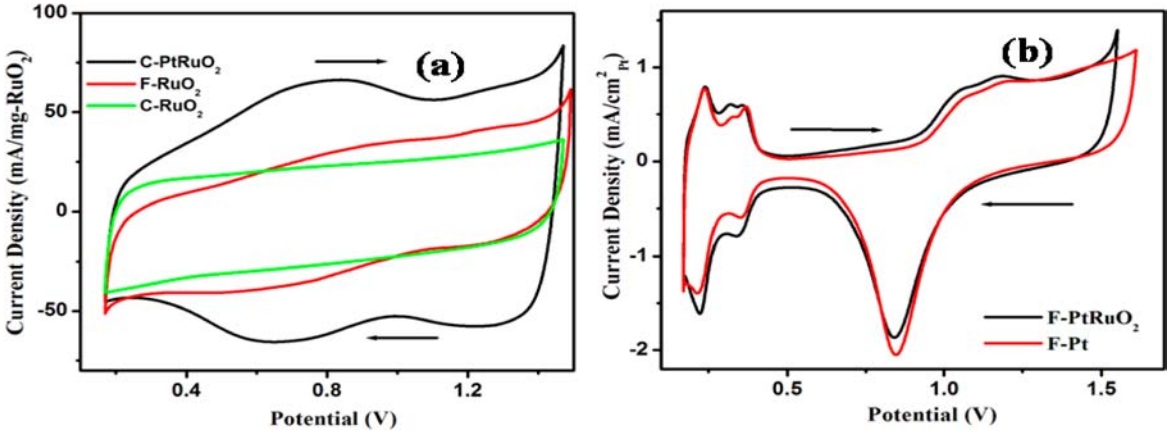

Figure 7. Comparison of the cyclic voltammograms of (a) C-$PtRuO_2$, C-RuO_2, and F-RuO_2 and (b) F-$PtRuO_2$ and F-Pt in 0.5 M H_2SO_4 taken at a scan rate of 50 mV/s vs NHE.

typical electrocatalytic behavior with respect to polycrystalline Pt.

To give additional evidence for the above observation, methanol oxidation is also carried out in a 1 M CH_3OH solution using 0.5 M H_2SO_4 as the supporting electrolyte. As shown in the CV traces presented in Figure 6a, distinct peaks that can be assigned to the oxidation of methanol are observed for F-$PtRuO_2$.[27] The tolerance factor obtained for this catalyst is 2.2, which shows the high tolerance of this material for CO poisoning. C-$PtRuO_2$ retains the rectangular shape in the CV even after the addition of CH_3OH. This indicates that C-$PtRuO_2$ is inactive toward methanol oxidation. This can be due to the increased capacitance contribution from the material, which suppresses the methanol oxidation current. These findings are in line with the observations from CV analysis in 0.5 M H_2SO_4, and it is thus assured that, in F-$PtRuO_2$, electrochemical attributes corresponding to Pt are obtained whereas C-$PtRuO_2$ sustained the characteristics of RuO_2.

Therefore, the results of the above electrochemical studies confirm that Pt is selectively exposed to the surface in F-$PtRuO_2$, while in C-$PtRuO_2$, mainly phase-separated, monometallic nanoparticles are formed. This unambiguous transition from the characteristic behavior of an electrocatalyst to the characteristic capacitive features for the same Pt:RuO_2 composition is a result of the controlled and predictable positioning of each component by virtue of the surface functional groups created during the pretreatment process.

Further, to demonstrate the promotional effect of the second counterpart in the performance characteristics of the single phase-pure analogue, we carried out CV analysis of pure Pt (F-Pt) and pure RuO_2 nanoparticles supported on CNF and FCNF (C-RuO_2 and F-RuO_2, respectively), and the resulting performances were compared with F-$PtRuO_2$ and C-$PtRuO_2$, respectively. A comparison of the cyclic voltammograms of C-$PtRuO_2$, C-RuO_2, and F-RuO_2 is displayed in Figure 7a. All of the materials display a rectangular CV loop with wide redox peaks. The specific capacitance values obtained (with respect to RuO_2 loading) for C-RuO_2 and F-RuO_2 are respectively 520 and 640 F/g, which are less compared to 1100 F/g obtained for C-$PtRuO_2$. Moreover, it can also be observed that the cyclic voltammogram corresponding to F-RuO_2 is slightly distorted, and it shows a deviation from the perfect rectangular shape. It is already reported in the literature that larger resistance distorts the loop, resulting in a narrower loop with an oblique angle.[26] From the previous literature reports, it can be inferred that the presence of Pt in the material reduces the resistance in the system and thereby increases the charge storage capability. F-$PtRuO_2$ also shows a remarkable enhancement in the electrochemical activity in the same manner as evidenced by the CV response given in Figure 7b. Although similar specific activities are obtained for both systems, the mass activity obtained for F-$PtRuO_2$ is considerably higher. The ECAS reaches 384 cm^2/mg of Pt for F-$PtRuO_2$ compared to 145 cm^2/mg of Pt obtained for F-Pt, which translates into an improvement factor of 2.6 for the bimetallic combination. Such an enhancement in the mass activity is reminiscent of the performance improvement brought about in the system by the addition of RuO_2, which could induce the preferential exposure of Pt to the surface coupled with the modifications in the atomic distributions resulting in a modified electronic structure of Pt in F-$PtRuO_2$.

■ CONCLUSIONS

We have demonstrated a simple covalent functionalization as a novel strategy to effectively tune the functionality of a hybrid material composed of Pt, RuO_2, and CNF from charge storage to electrocatalysis. This is achieved by a controlled and predictable assembly of the desired nanoparticles based on the fundamental concept of the preferential adsorption of ions. The microscopic characterization strongly points toward this architectural tuning effected in the system, which is also supported by XPS analysis. The clear transition from the characteristic capacitor behavior to the typical electrocatalytic activity is demonstrated using electrochemical analysis. Such a switchover in the property while moving from the pristine CNF to the activated CNF, for the same composition of Pt and RuO_2, is by virtue of the predetermined positioning of the individual components on the CNF support. This is achieved based on the preferential adsorption of one metal ion over the other due to the presence of functional groups created after the activation process. Because functionalization of carbon nanostructures is well documented in the literature to create various functional groups like −SH, $-NH_2$, $-SO_3H$, etc., we envision that this strategy can be potentially extended for organizing various nanoparticles at our desire.

dx.doi.org/10.1021/ic301147s | Inorg. Chem. 2012, 51, 9766−9774

■ ASSOCIATED CONTENT

Supporting Information

EDX spectra of F-$PtRuO_2$ and C-$PtRuO_2$, IR spectra of CNF and FCNF, and CV of C-$PtRuO_2$ and CNF at various scan rates. This material is available free of charge via the Internet at http://pubs.acs.org.

■ AUTHOR INFORMATION

Corresponding Author

*E-mail: k.sreekumar@ncl.res.in. Tel: +91-20-25902566. Fax: (+91)-20-2590-2636.

Notes

The authors declare no competing financial interest.

■ ACKNOWLEDGMENTS

B.K.B. gratefully acknowledges the Council of Scientific and Industrial Research (CSIR), New Delhi, India, for a Junior Research Fellowship. Financial support of the CSIR through the network programme is gratefully acknowledged. Anuj S. Pokle and Pandiaraj S are thanked for HRTEM imaging. Dr. K. Vijayamohanan is thanked for his contributions.

■ REFERENCES

(1) Wei, Z.; Kondratenko, M.; Dao, L. H.; Perepichka, D. F. *J. Am. Chem. Soc.* **2006**, *128*, 3134−3135.
(2) Qi, P.; Vermesh, O.; Grecu, M.; Javey, A.; Wang, Q.; Dai, H. *Nano Lett.* **2003**, *3*, 347−351.
(3) Wang, J.; Liu, G.; Jan, M. R. *J. Am. Chem. Soc.* **2004**, *126*, 3010−3011.
(4) Niyogi, S.; Hamon, M. A.; Hu, H.; Zhao, B.; Bhowmik, P.; Sen, R.; Itkis, M. E.; Haddon, R. C. *Acc. Chem. Res.* **2002**, *35*, 1105−1113.
(5) Balasubramanian, K.; Burghard, M. *Small* **2005**, *1*, 180−192.
(6) Hirsch, A. *Angew. Chem., Int. Ed.* **2002**, *41*, 1853−1859.
(7) Peng, H.; Alemany, L. B.; Margrave, J. L.; Khabashesku, V. N. *J. Am. Chem. Soc.* **2003**, *125*, 15174−15182.
(8) Okamoto, M.; Fujigaya, T.; Nakashima, N. *Adv. Funct. Mater.* **2008**, *18*, 1776−1782.
(9) Williams, K. A.; Veenhuizen, P. T. M.; Torre, B. G.; Eritja, R.; Dekker, C. *Nature* **2002**, *420*, 761−762.
(10) Taberna, P. L.; Mitra, S.; Poizot, P.; Simon, P.; Tarascon, J. M. *Nat. Mater.* **2006**, *5*, 567−573.
(11) Liu, R.; Lee, S. B. *J. Am. Chem. Soc.* **2008**, *130*, 2942−2943.
(12) Balan, B. K.; Unni, S. M.; Kurungot, S. *J. Phys. Chem. C* **2009**, *113*, 17572−17578.
(13) Iwakura, C.; Hirao, K.; Tamura, H. *Electrochim. Acta* **1977**, *22*, 329−334.
(14) Balan, B. K.; Kurungot, S. *J. Mater. Chem.* **2011**, *21*, 19039−19048.
(15) Tibbetts, G. G.; Doll, G. L.; Gorkiewicz, D. W.; Moleski, J. J.; Perry, T. A.; Dasch, C. J.; Mkchael, J. B. *Carbon* **1993**, *31*, 1039−1047.
(16) Paredes, J. I.; Burghard, M.; Martínez-Alonso, A.; Tascón, J. M. D. *Appl. Phys. A: Mater. Sci. Process.* **2005**, *80*, 675−682.
(17) Carneiro, O. C.; Kim, M. S.; Yim, J. B.; Rodrigue, N. M.; Baker, R. T. K. *J. Phys. Chem. B* **2003**, *107*, 4237−4244.
(18) Kijima, T.; Nagatomo, Y.; Takemoto, H.; Uota, M.; Fujikawa, D.; Sekiya, Y.; Kishishita, T.; Shimoda, M.; Yoshimura, T.; Kawasaki, H.; Sakai, G. *Adv. Funct. Mater.* **2009**, *19*, 545−553.
(19) Alayoglu, S.; Nilekar, A. U.; Mavrikakis, M.; Eichhorn, B. *Nat. Mater.* **2008**, *7*, 333−338.
(20) Gebhardt, B.; Syrgiannis, Z.; Backes, C.; Graupner, R.; Hauke, F.; Hirsch, A. *J. Am. Chem. Soc.* **2011**, *133*, 7985−7995.
(21) Fu, R.; Zeng, H.; Lu, Y.; Lai, S. Y.; Chan, W. H.; Ng, C. F. *Carbon* **1995**, *33*, 657−661.
(22) Foelske, A.; Barbieri, O.; Hahn, M.; Kötz, R. *Electrochem. Solid-State Lett.* **2006**, *9*, A268−A272.
(23) Li, X.; Park, S.; Popov, B. N. *J. Power Sources* **2010**, *195*, 445−542.
(24) Parkinson, C. R.; Walker, M.; McConville, C. F. *Surf. Sci.* **2003**, *545*, 19−33.
(25) Bi, R. R.; Wu, X. L.; Cao, F. F.; Jiang, L. Y.; Guo, Y. G.; Wan, L. J. *J. Phys. Chem. C* **2010**, *114*, 2448−2451.
(26) Shaijumon, M. M.; Ou, F. S.; Ciab, L.; Ajayan, P. M. *Chem. Commun.* **2008**, *20*, 2373−2375.
(27) Susut, C.; Chapman, G. B.; Samjeske, G.; Osawac, M.; Tong, Y. *Phys. Chem. Chem. Phys.* **2008**, *10*, 3712−3721.
(28) Wang, C.; Daimon, H.; Onodera, T.; Koda, T.; Sun, S. *Angew. Chem.* **2008**, *120*, 3644−3647.